Local band bending and grain-to-grain interaction induced strain nonuniformity in polycrystalline CdTe films

V. Consonni,[1,*] N. Baier,[2] O. Robach,[3] C. Cayron,[4] F. Donatini,[5] and G. Feuillet[2]

[1]*Laboratoire des Matériaux et du Génie Physique, CNRS–Grenoble INP, 3, parvis Louis Néel, 38016 Grenoble, France*
[2]*CEA-LETI, Minatec Campus, 17 rue des Martyrs 38054 Grenoble, France*
[3]*CEA-INAC, 17 rue des Martyrs 38054 Grenoble, France*
[4]*CEA-LITEN, 17 rue des Martyrs 38054 Grenoble, France*
[5]*Institut Louis Néel, CNRS–Université Joseph Fourier, 25 rue des Martyrs 38042 Grenoble, France*

The local physical properties of polycrystalline semiconducting films drive their performances in a wide variety of optoelectronic devices but are still not completely elucidated. These properties are investigated and correlated on the same region of polycrystalline CdTe films by combining electron backscattered diffraction, μ-Laue x-ray experiments using synchrotron radiation, electron beam-induced current, and cathodoluminescence. The local band bending is revealed at random grain boundaries: its characteristics vary from one grain to another, depending on the nature of grain boundaries and the doping level in the nearby grains, in agreement with the theoretical approach of the double Schottky potential barriers. In contrast, no local band bending occurs at $\Sigma3$ growth twins since these extended defects have no dangling bonds in their center. Additionally, the density of unpaired dislocations and the components of the strain and stress tensors are found to be highly nonuniform from one grain to another and within the grains themselves. This reveals that grain-to-grain interactions (i.e., collective effects) occur during the Volmer-Weber-type growth. These findings emphasize the critical importance of grain boundary design engineering. They also highlight how polycrystalline semiconducting films work locally and show the complexity of the local physical processes governing their macroscopic performances in optoelectronic devices.

PACS number(s): 73.61.Ga, 78.66.Hf, 68.55.ag, 68.60.Bs

I. INTRODUCTION

The use of polycrystalline compound semiconductors (SCs) as thin or thick active layers has received, in the past few decades, increasing interest for a wide variety of emerging chemical, physical, mechanical, electronic, or optical devices [1,2]. Polycrystalline compound SC films can be considered as cheap and versatile bulk SCs. Their growth is driven by the Volmer-Weber-type mechanism [3]: isolated three-dimensional (3D) islands nucleate on the substrate surface, coarsen, and then coalesce. Island coalescence results in the formation of grain boundaries (GBs): these planar extended defects accommodate the crystalline lattice between the neighboring grains, leading to the occurrence of spatially inhomogeneous chemical, electrical, and optical properties [4,5]. GBs typically present a large number of defects owing to incomplete atomic bonding, resulting in the detrimental formation of deep levels in the band gap [6–9]. They are electrically charged after trapping the charge carriers. The local band bending at GBs and, hence, the occurrence of electrostatic potential barriers have widely been reported for polycrystalline Si and ZnO films [6,7] and modeled in the framework of the double Schottky potential barriers both in n- or p-type SCs [4–9]. As a rule, polycrystalline compound SC films offer several very specific physical properties owing to the presence of GBs, which can either be detrimental or beneficial for the devices.

A good example of how a compound SC in its polycrystalline variant can somehow outperform its monocrystalline variant is illustrated in the case of polycrystalline CdTe films [10,11]. Polycrystalline CdTe films are building blocks for cost-efficient electronic and optical devices, where very large dimensions are required, such as solar cells or γ- and x-ray detectors [12–14]. Thorpe *et al.* have revealed by macroscopic electrical measurements the hole depletion near GBs in CdTe bicrystals [15]. The physical properties of GBs have further been investigated in polycrystalline CdTe films by optical reflectance and transmittance measurements [16,17]. Romero *et al.* have shown by cathodoluminescence (CL) imaging that the density of impurity states is larger at GBs than in the interior of grains, leading to the occurrence of electric fields surrounding the GBs [18]. The segregation of chlorine atoms acting as dopants has been found to occur in the vicinity of GBs by time-of-flight secondary ion mass spectrometry, leading to nonuniform doping and optical properties as well as drag phenomena during grain growth [19–21]. Visoly-Fisher *et al.* [10,11,22] have found by scanning capacitance measurements and scanning Kelvin probe measurements that a barrier for hole transport occurs across GBs, indicating the local band bending at GBs. This has been confirmed by scanning tunneling microscopy and near-field optical beam-induced current measurements [23,24]. The resulting electron conduction enhancement at GBs is expected to be beneficial for solar cells, although leading to nonuniform electrical properties [10,11,23–25]. However, the previous analysis has been achieved very locally: no statistical measurements over a large population of GBs have, so far, been reported, whereas the physical phenomenon is expected to strongly depend on the nature of GBs or the orientation of the nearby grains, for instance. In addition, only very few works have been devoted to revealing the spatial distribution

---

*Corresponding author: vincent.consonni@grenoble-inp.fr

of stress in polycrystalline materials, especially by μ-Laue x-ray experiments using synchrotron radiation [26]: the stress in polycrystalline Al and Cu films has been found to be highly inhomogeneous [26–28]. This has never been investigated in polycrystalline CdTe films, although this could play a major role in its physical properties.

In this paper, we investigate and correlate on the local scale the structural and electro-optical properties of polycrystalline CdTe films by combining electron backscattered diffraction (EBSD) and μ-Laue x-ray experiments using synchrotron radiation with electron beam-induced current (EBIC) and CL imaging. The whole study of the structural and electro-optical properties has been carried out on the same region of polycrystalline CdTe films.

II. EXPERIMENT

Polycrystalline CdTe films were grown by close space sublimation (CSS) of a source material composed of a mixture of $CdCl_2$ and CdTe powders on a graphite substrate [21]. The source and substrate temperatures were 600 and 500 °C, respectively. The growth rate of polycrystalline CdTe films is large by CSS and typically about 300 μm/h, thus preventing any epitaxial relationship from establishing with the substrate. Prior to the experimental data collection, the samples were marked by basic photolithography such that the investigated zone could clearly be identified: EBIC, EBSD, CL, and μ-Laue x-ray measurements were therefore performed on the same region of the polycrystalline CdTe film. This permits a direct correlation of the structural and electro-optical properties on the local scale.

EBSD measurements were recorded with a 1530 ZEISS scanning electron microscope (SEM), while EBIC and CL measurements were performed with a Quanta 200 FEI SEM. The electron-hole pair formation energy is 4.56 eV in CdTe, indicating that the energy is roughly lost within a probing volume with a projected radius on the surface of about 4 μm. For the EBIC measurements, gold electrodes were deposited on each side of the CdTe films through an electroless process in $AuCl_3$ solution. The applied electric bias is in the range of 20 to 100 V. In our EBIC configuration, only electron drift is concerned since the $\mu\tau$ product of the hole mobility μ and lifetime τ (characterizing the mean path length) is about 20 times smaller than for electrons. By considering that the probing volume is greater than the spot size and that the projected radius on the surface is about 4 μm, the induced current spreads over a maximum range of about 1 μm. The EBIC current is calibrated as the difference with its average value of 500 nA determined on the largest map, which is put to 0 by convention. The CL signal was detected with a monochromator coupled to a multialkali photomultiplier tube.

The general description of the set-up for μ-Laue x-ray experiments on the BM32 beam line at the European Synchrotron Radiation Facility (ESRF) is given in Ref. [29]. The size of the white x-ray beam was of 0.5×2.2 μm^2, and its energy was in the range of 5 to 22 keV. The approximate probe volume is a cylinder of $0.5 \times 2.2 \times L_1$ μm^3, and the axis is at 40° from the sample surface. L_1 varies with the *hkl* diffraction spot and energy and is in the range of 2 to 100 μm. The μ-Laue patterns were recorded over a square area of 400×400 μm^2 with a step

size of 5×5 μm^2 and a collection time of 0.12 s. The experimental data analysis for the μ-Laue x-ray measurements was achieved with the homemade open-source software LaueTools developed by Micha and Robach at ESRF [30]. As the CdTe polycrystalline film is irradiated by a white x-ray beam, with a typical size of 0.5×2.2 μm^2 (i.e., smaller than grain size), the diffraction patterns are Laue diagrams, as in the case of single crystalline materials. Since the CdTe polycrystalline film is mounted in the reflection geometry, the diffraction spots are distributed along hyperbolae representing the zone axis. By scanning the sample in front of the microbeam along the x, y directions, the maps of the pixel mean deviation, the local misorientation angle, and the components of the deviatoric strain tensor can be collected within each grain. The pixel mean deviation is the mean distance between the experimental and theoretical spot positions in the μ-Laue diagrams. The experimental spot positions are refined according to a simple model of rotation and elastic strain of the primitive lattice. The regions of high pixel mean deviation are related to the presence of a high density of defects (i.e., stacking faults), shifting the experimental spot positions from their theoretical positions. For the maps of the local misorientation angle, the mean orientation is calculated by averaging the components of the orientation matrices, giving the vector coordinates (a*,b*,c*). The regions of large variation of the local misorientation angle correspond to the presence of a high density of unpaired dislocations (i.e., plastic strain gradient). The maps are refined from N spots, with N being in the range of 20 to 95. The highly precise calibration of the experiment geometry is achieved thanks to the μ-Laue pattern of Ge single crystal. This allows the determination of the absolute value of the angles of the diffraction vector, which results in the absolute measurement of the local deviatoric lattice parameters (α, β, γ, b/a, c/a). The deviatoric strain tensor is converted into the deviatoric stress tensor by applying the matrix Hooke's relation, from which an elastic constant tensor is used with the values given in Ref. [31]. It should be noted that the (small) average of each strain tensor component as determined on the full set of grains of the 400×400 μm^2 map is subtracted in order to compensate a possible systematic error related to the experimental uncertainties of the experiment geometry.

III. RESULTS AND DISCUSSION

A. Structural morphology and luminescence at the local scale

The polycrystalline CdTe film has a typical thickness of about 350 μm and consists of grains with a diameter of several tens of micrometers. The structural morphology is strongly dependent upon the film thickness as shown in Fig. 1 and hence upon the formation mechanisms following the Volmer-Weber-type growth related to the strong anisotropy of CdTe. At the onset of the nucleation phase, isolated 3D islands nucleate on the substrate surface and are slightly oriented along the $\langle 111 \rangle$ direction owing to surface energy minimization: the {111} planes have the lowest surface energy in the zinc blend crystalline structure of CdTe [31]. Subsequently, isolated 3D islands coarsen. The phase of island coalescence leads to the formation of GBs arising from attractive forces between nearby islands. Typically, high tensile biaxial stress is generated: the
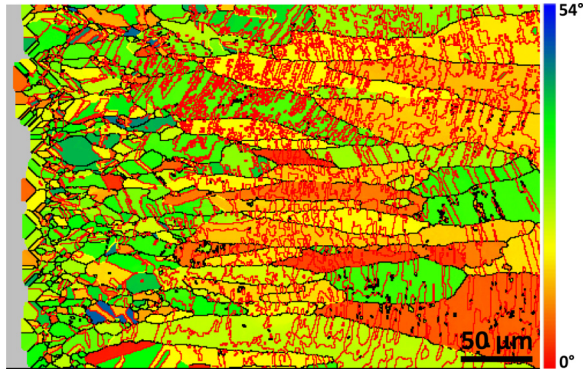
FIG. 1. (Color online) (a) Cross-sectional view EBSD orientation map of the polycrystalline CdTe film. The color scale denotes the angular deviation from the $\langle 111 \rangle$ crystallographic direction along the growth axis. The substrate is located on the left. The $\Sigma 3$ twins are indicated in red.

stress magnitude of several tens of megapascals has been determined by conventional x-ray diffraction measurements on CdTe coalesced islands [31]. This is correlated with the occurrence of $\langle 531 \rangle$, $\langle 100 \rangle$, and $\langle 110 \rangle$ preferential orientations related to strain energy minimization [31]. The grains are, therefore, formed and stacked in a continuous two-dimensional film for the film thickness below 80–100 μm, as presented in Fig. 1: they only present a slight texture, owing to thermodynamic considerations as the process of abnormal grain growth occurs, and also undergo a strong evolution of biaxial stress state from tensile to compressive stress [31]. Furthermore, it should be noted that their size and shape is highly dispersed, as presented in Fig. 1. Eventually, larger columnar grains are formed on top of slightly textured smaller stacked grains at a film thickness of about 80–100 μm, following the phase of secondary nucleation, as revealed in Fig. 1. The physical origin for the formation and development of large columnar grains is still not completely understood. Very likely, the secondary nucleation on top of preexisting CdTe stacked grains should be distinguished from the primary nucleation on top of the substrate surface and is favorable for the formation of large columnar grains. Similarly to stacked grains, the size and shape of columnar grains is strongly dispersed. Also, their development is highly competitive in the polycrystalline CdTe film, as indicated, for instance, by the occlusion of several columnar grains in Fig. 1. The columnar grains are mostly oriented along the $\langle 111 \rangle$ direction, as shown in Figs. 1, 2(a), and 2(d). For large film thickness of several hundreds of micrometers, the texture of columnar grains is related instead to kinetics considerations: the growth rate is faster on the planes other than the (111) planes, but their growth is subsequently limited by the development of slow growing (111) facets [31]. Additionally, a high density of $\Sigma 3$ growth twins with a small thickness is revealed in the image of the twin-related domains (TRDs) shown in Fig. 2(c), as reconstructed with the homemade software ARPGE [32]. $\Sigma 3$ indicates that the coincidence is made only for one-third of the lattice sites: the two subgrains adjacent to the (111) twin plane are related by a 180° rotational symmetry around the [111] direction. In the TRDs, each subgrain is connected by a chain of $\Sigma 3$ twins (i.e., $\Sigma 3^n$ operators where n is an integer).

The twins lie within TRDs of any $\langle hkl \rangle$ orientation and end either in the interior of the grains or at GBs, delineating a wavy substructure. In contrast, $\Sigma 3$ deformation twins occur in the interior of stacked grains at the film thickness below 80–100 μm and systematically end at GBs, as shown in Fig. 1. While $\Sigma 3$ deformation twins are expected to form in the course of island coalescence that generates a high tensile biaxial stress [33], $\Sigma 3$ growth twins may subsequently nucleate owing to the low stacking fault formation energy of 16 mJ/m^2 in CdTe [34]. Besides the $\Sigma 3$ growth twins, a low density of $\Sigma 9$ (i.e., $\Sigma 3^2$), $\Sigma 27$ (i.e., $\Sigma 3^3$), and $\Sigma 81$ (i.e., $\Sigma 3^4$) twins is also revealed in Fig. 2(c). Their proportion is low as compared to other materials with low stacking fault formation energy, indicating that the growth twinning of CdTe is mainly polysynthetic [32]. Furthermore, apart from $\Sigma 3$ growth twins, the polycrystalline CdTe film presents a wide variety of low-symmetry high-angle (i.e., random) GBs delineating the grain structure, as expected in polycrystalline SC films grown by low-cost physical vapor deposition techniques, which leads to a large dispersion of the nature of GBs. These random GBs, seen as dark regions in the CL image of Fig. 3(d), act as preferential nonradiative recombination centers, indicating the presence of trap states [35]. In contrast, the luminescence, seen as bright regions, mainly comes from the interior of the grains but is also very inhomogeneous. The presence of dark regions, and thus of nonradiative recombination centers within the grains themselves, is clearly revealed. Importantly, the high density of $\Sigma 3$ growth twins, as indicated in the EBSD orientation maps [red lines of Figs. 3(a) and 3(b)], is somehow correlated with the dark regions of the CL image in Fig. 3(d). More precisely, although the $\Sigma 3$ growth twins are free of dangling bonds and free of strain and hence should not act as efficient nonradiative recombination centers, their edges [i.e., the so-called double-positioning twin boundaries (DPBs)] lying in the $\{11\bar{2}\}$ planes present a wide number of dangling bonds [36]. When a twin ends in the interior of the grain, a DPB is systematically formed. Accordingly, the role of DPBs is expected to be significant in the inhomogeneous spatial distribution of luminescence within the grains [35]. Additionally, the presence of dislocations may also strongly affect the spatial distribution of luminescence.

B. Local band bending at random and specific GBs

In weakly chlorine-doped polycrystalline CdTe films, the interior of the grains is generally of p-type: although the chlorine atoms substitute for tellurium and act as donors, the formation of acceptor complexes involving cadmium vacancies (i.e., the so-called A centers and β complexes) are predominant, as revealed in CL measurements [19,20,33]. These grains are separated by presumably positively charged random GBs. According to the theoretical model of the double Schottky potential barriers, by solving Poisson's equation, the electrostatic potential barrier height Φ_B at GBs and the depletion layer width d are at zero bias given by [4–9] $\Phi_B = Q_i^2 / 8e\varepsilon_0\varepsilon_r N_0$ and $d = Q_i / 2N_0$, where $Q_i = eN_t$ is the net surface charge, e is the elementary charge, N_t is the surface density of trapped charge carriers, N_0 is the volume density of ionized acceptors in the grains, ε_r is the static dielectric
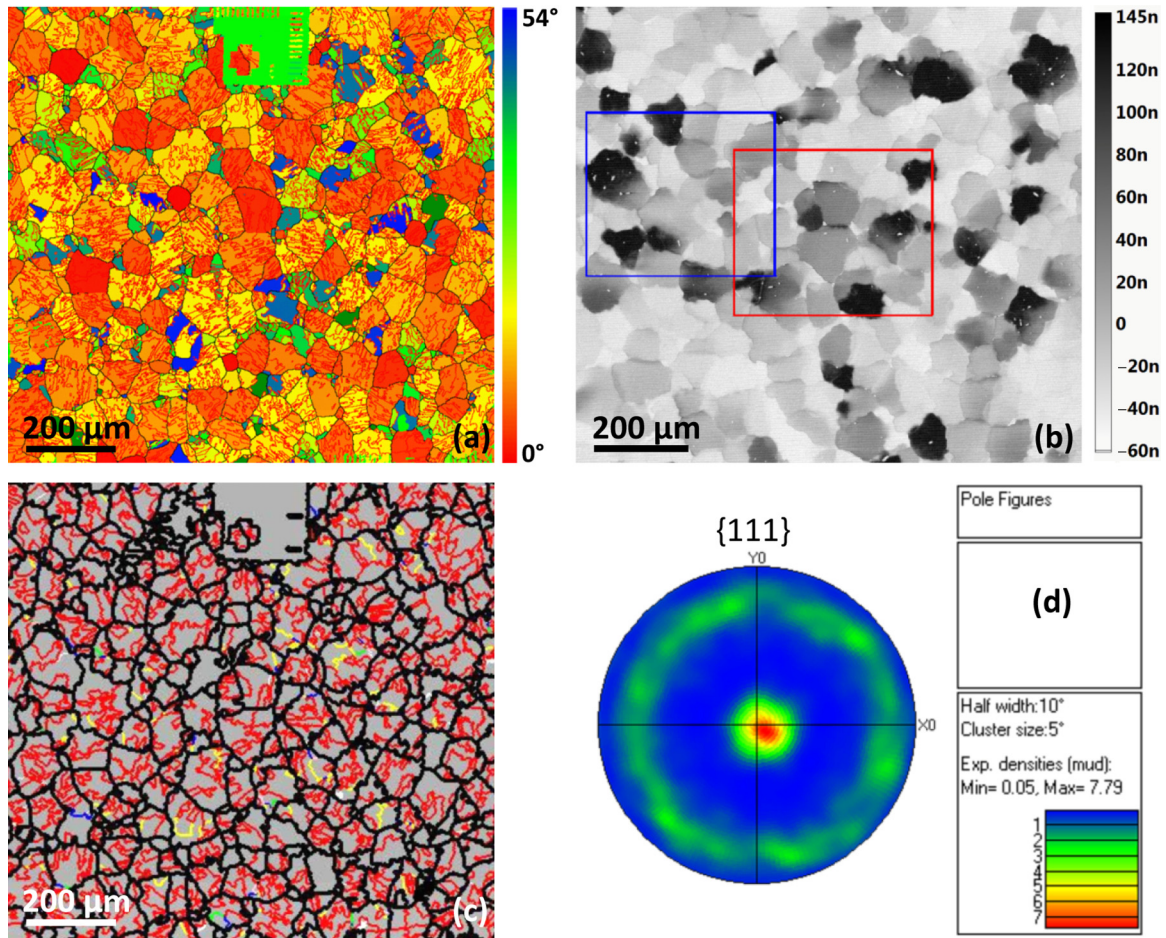
FIG. 2. (Color online) (a) EBSD orientation map of the polycrystalline CdTe film. The color scale denotes the angular deviation from the ⟨111⟩ crystallographic direction along the growth axis. (b) EBIC image of the same region of the polycrystalline CdTe film. The EBIC current is collected at the applied electric bias of 30 V and calibrated as the difference with its average value determined on the largest map, which is set to 0 by convention. The EBIC current unit is in nanoamperes. The red and blue rectangular areas indicate the spatial positions of Fig. 3. Note that the intensity of EBIC current is increased from white to black colors (c) Corresponding EBSD image showing the multi-TRDs with $\Sigma 3$ twins in red, $\Sigma 9$ twins in yellow, $\Sigma 27$ twins in blue, and $\Sigma 81$ twins in green. (d) Corresponding EBSD pole figure along the ⟨111⟩ crystallographic orientation.

constant, and ε_0 is the vacuum permittivity. For the sake of determining orders of magnitude, the barrier is assumed to be symmetrical. By taking $N_t = 10^{12}$ cm^{-2} (i.e., a typical value for GBs in CdTe) [16,17], $N_0 = 10^{17}$ cm^{-3} (i.e., a typical value for chlorine doping in CdTe) [33], and $\varepsilon_r = 10.16$ [37], $\Phi_B = 0.22$ V and $d \sim 100$ nm at zero bias, which corresponds to the order of magnitude reported for polycrystalline CdTe films [16,17,38].

Here, the local band bending of polycrystalline CdTe films is investigated by EBIC measurements. The EBIC measurements performed on the same region of the polycrystalline CdTe film are presented in Figs. 2(b), 3(c), 4(b), and 4(d) and reveal important physical effects. The induced current on the electrodes generated by electron drift under the effect of the applied electric field is strongly nonuniform [39]. First, the nonuniformity of the induced current is shown from one grain to the other and does not appear to be correlated to their size, shape, and orientation. This specifically indicates that the EBIC measurements are not governed by the contact property between the polycrystalline CdTe and gold contact.

In contrast, the position of the quasi Fermi level and hence the magnitude of the induced current from one grain to the other is strongly dependent upon the volume density of ionized acceptors in the nearby grains. Although the chlorine atoms looks, on a microscopic scale, fairly uniform in the interior of the grains [19,20,33], the density of extended defects acting as traps or recombination centers is likely to vary. Moreover, the density of dislocations or DPBs can affect the efficiency of the chlorine doping on the local scale, resulting in the variation of the induced current, as shown in Figs. 2(b), 3(c), 4(b), and 4(d) from one grain to the other. It seems that the grains with a high induced current have a low density of DPBs in their center, as shown in Fig. 3: the high induced current is indeed related to a small depletion layer width and hence to a small volume density of ionized acceptors in the grains. It is also worth noticing that the profile of the electrostatic potential barrier height is asymmetrical in Fig. 4(e), which can also originate from the difference in the volume density of ionized acceptors from one grain to the other. Second, an increase in the induced current mainly occurs in the vicinity of
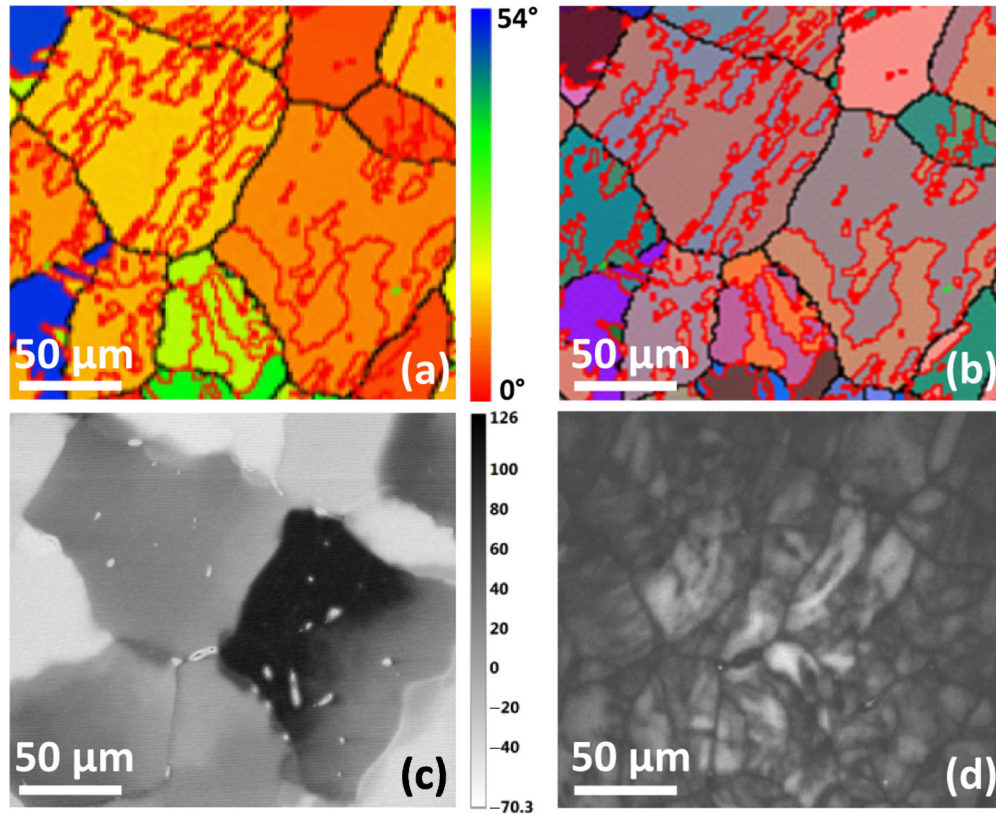
FIG. 3. (Color online) (a) EBSD orientation map of the polycrystalline CdTe film. The color scale denotes the angular deviation from the $\langle 111 \rangle$ crystallographic direction along the growth axis. (b) Corresponding EBSD image in Euler angles with arbitrary colors. (c) EBIC image and (d) panchromatic CL image of the same region of the polycrystalline CdTe film. Note that the intensity of EBIC current is increased from white to black colors.

some of the GBs as revealed in Figs. 2(b), 3(c), 4(b), and 4(d): both the magnitude of the jump of the induced current and its extension vary from one GB to the other. The random GBs in the polycrystalline CdTe film contribute to the local band bending, [10,11,16,17,22–25], which, in turn, leads to an increase in the electron density and thus in the jump of the induced current in their vicinity. The induced current spreads over a maximum length of about 1 μm by considering the probing volume and the projected radius, which is still fairly large as compared to the theoretical value and comes from the large diffusion of electrons deteriorating the spatial resolution of the EBIC measurements. According to the theoretical model of the double Schottky potential barriers, the electrostatic potential barrier height and the depletion layer width strongly depend on the surface density of trapped charge carriers (i.e., the surface density of traps) at GBs and hence on the nature of GBs involved, such as its misorientation, plane, and energy. In principle, it is expected that the surface density of traps at GBs increases with a loss of symmetry or by increasing its misorientation. In fact, the local band bending occurs at all random GBs but is visible only at some of the GBs in EBIC measurements since its spatial resolution, as well as its current sensitivity, is limited. The wide variety of random GBs, as shown in Figs. 2(a), 3(a), 4(a), and 4(c), accounts for the different characteristics of the local band bending. For instance, in Figs. 4(b) and 4(d), the GBs are misoriented by high angles of 38 and 23° around the $\langle 323 \rangle$ and $\langle 313 \rangle$

orientations, respectively, and should present a high surface density of traps. This leads to the significant jump of 20 to 30 nA of the induced current, as presented in Fig. 4(e), correlated with an important local band bending. In contrast and more importantly, the $\Sigma 3$ growth twins, being free of any dangling bonds and hence of traps, do not result in a variation of the induced current and in a local band bending, which is in agreement with the theoretical model of the double Schottky potential barriers.

C. Grain-to-grain interaction induced strain nonuniformity

In order to correlate such local structural and electro-optical properties with a local strain and stress analysis, μ-Laue x-ray experiments were performed on the same region of the polycrystalline CdTe film in BM32 beam line at ESRF. The general description of the beam line setup is given in Ref. [29]. As the polycrystalline CdTe film is irradiated by a white x-ray microbeam smaller than grain size, the μ-Laue patterns are Laue diagrams, as in the case of single-crystalline materials. The μ-Laue patterns are collected over a variable film thickness in the range from 2 to 100 μm, depending on the *hkl* diffraction spots: however, despite the variable film thickness probed, they are recorded in the region of columnar grains, as shown in the EBSD image of Fig. 1. The μ-Laue spots are distributed along hyperbolae representing the zone axis owing to the reflection geometry, as shown in
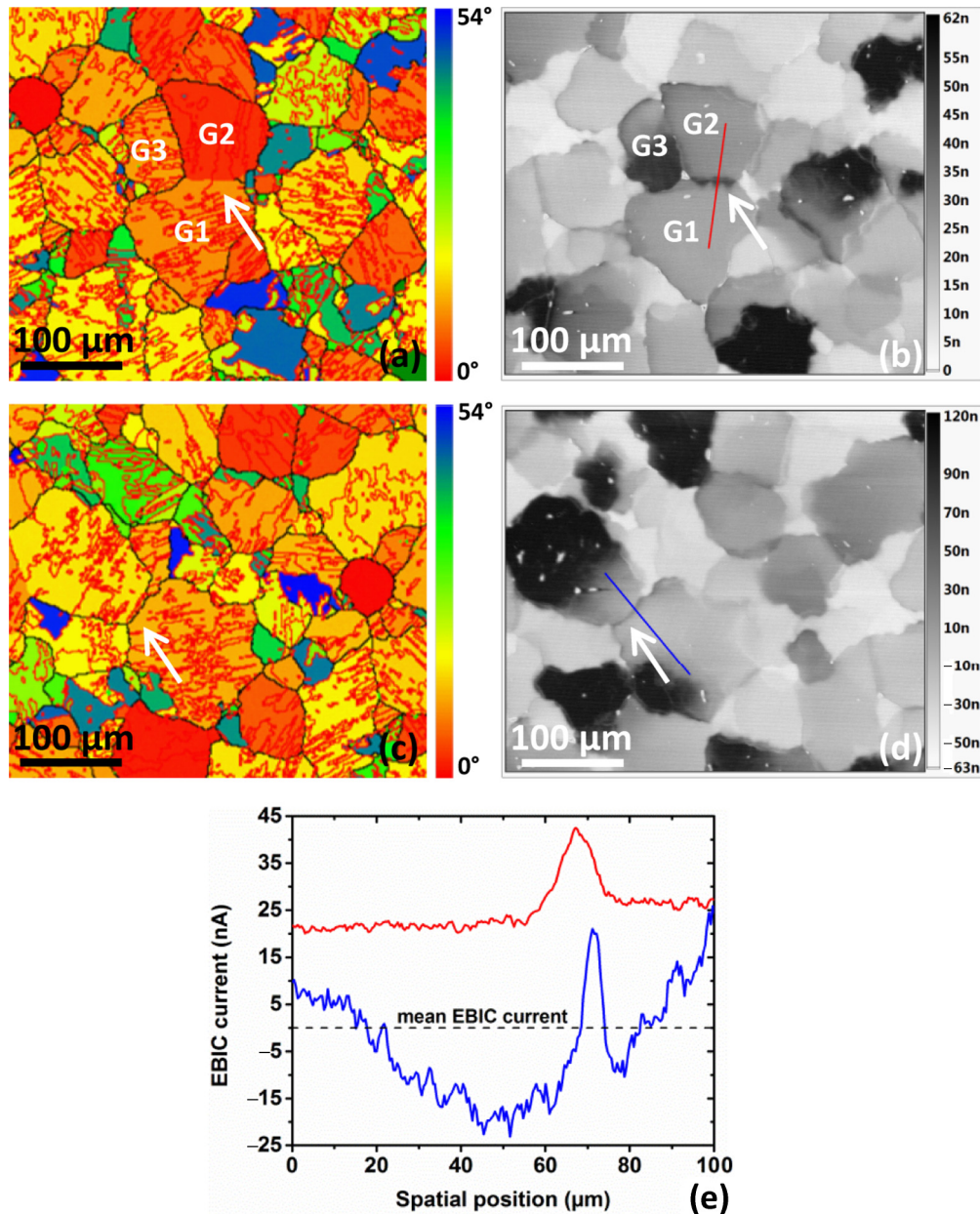
FIG. 4. (Color online) (a) and (c) EBSD orientation maps and (b) and (d) EBIC images of the same region of the polycrystalline CdTe film, respectively. The EBIC current is collected at the applied electric bias of 30 V and calibrated as the difference with its average value determined on the largest map, which is set to 0 by convention. The EBIC current unit is in nanoamperes. Note that the intensity of EBIC current is increased from white to black colors. (e) Profile of the EBIC signal around random GBs in the polycrystalline CdTe film. The profile is achieved according to the red and blue lines in (b) and (d), respectively. The GBs considered are indicated by the white arrows in (a)–(d), respectively. The GBs in (a)–(d) are misoriented by high angles of 38 and 23° around the $\langle 323 \rangle$ and $\langle 313 \rangle$ orientations, respectively. The grains G1, G2, and G3 are located in (a) and (b) for the μ-Laue x-ray experiment analysis.

Fig. 5(a). Basically, the μ-Laue diagrams superimpose the spots originating from primary and secondary grains oriented along the $\langle 111 \rangle$ growth axis [i.e., G1 and G1′, for instance, in Figs. 5(a) and 5(b)], with the secondary grains being in $\Sigma 3$ twin relationship with the primary grains. About one out of three spots (i.e., the so-called multitwinned spots) belongs to both primary and secondary grains. The maps of the pixel mean deviation provide an estimate of the spatial distribution of defects (i.e., stacking faults). They are highly inhomogeneous in the interior of primary grains G1, G2, and

G3, as revealed in Fig. 5(d). Additionally, the maps of the local misorientation angle, whose the gradient provides the spatial distribution of unpaired dislocations, are also nonuniform in primary grains G1, G2, and G3, as shown in Fig. 5(e). A high density of unpaired dislocations arises at the bottom right of grain G3: this region may be correlated with the high induced current in Fig. 4(b). Interestingly, a high density of unpaired dislocations is also pointed out in the vicinity of random GBs at the bottom left of grain G1, where a high induced current arises in Fig. 4(b). Importantly, the variation of the density of
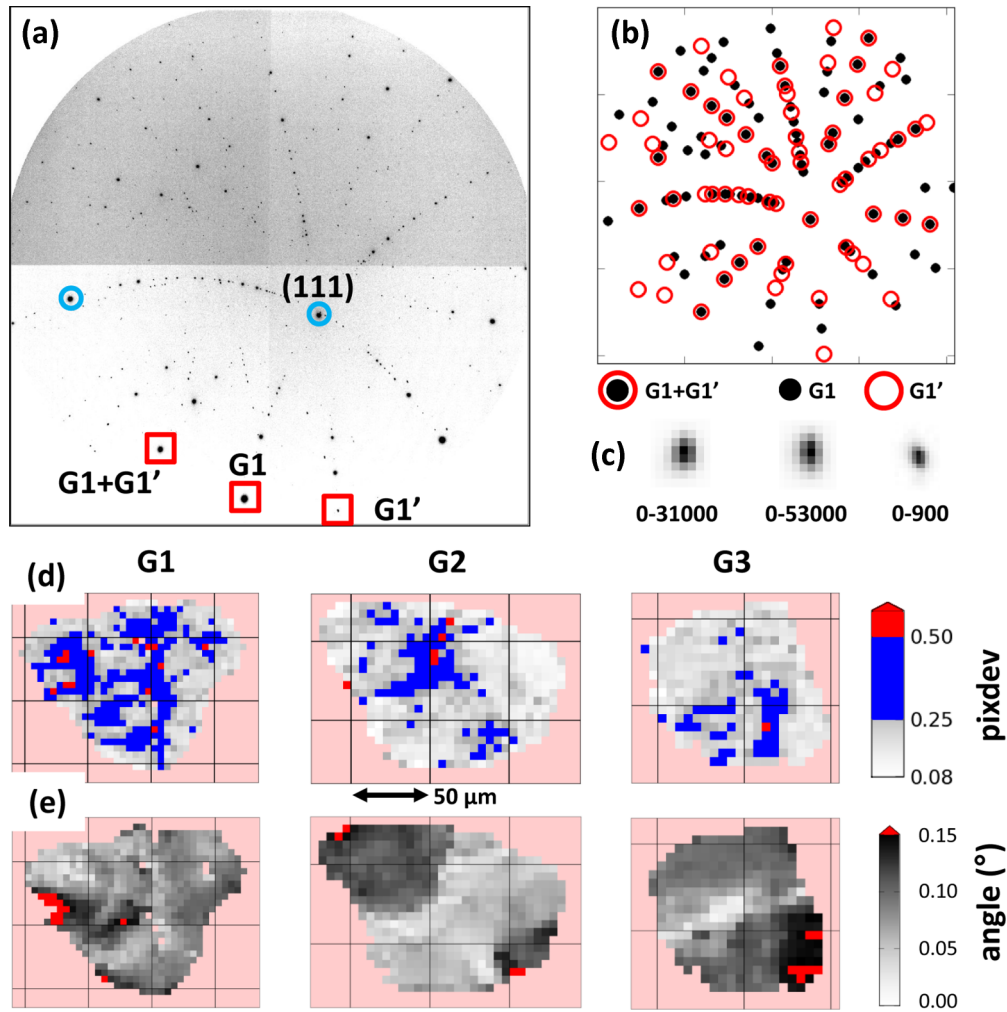
FIG. 5. (Color online) (a) μ-Laue x-ray diagram of two typical grains, denoted G1 and G1′, located at the center of Figs. 3(a) and 3(b) and oriented along the $\langle 111 \rangle$ growth axis. G1 and G1′ are the primary and secondary grains, respectively; G1 and G1′ are in $\Sigma 3$ twin relationship. These two grains occupy a similar surface area in the different maps. (b) Position of primary grain G1 spots (black dots) and of secondary grain G1′ spots (red circle). One out of three spots belongs to both primary grain G1 and secondary grain G1′ spots (multitwinned spots). (c) High magnification of the spots framed in red in (a). A good estimate for the position of their mass center is favored by the simple spot shape, allowing good accuracy for strain and stress calculations. (d) Maps of the pixel mean deviation (i.e., pixdev) between the experimental and theoretical spot positions in the μ-Laue x-ray diagram for primary grains G1, G2, and G3. (e) Maps of the local misorientation angle with respect to the mean orientation for primary grains G1, G2, and G3. The maps for secondary grains G1′, G2′, and G3′ (not shown here) are very similar.

unpaired dislocations is likely to affect the spatial distribution of dopants through segregation phenomena for instance. This could, therefore, influence the local band bending at random GBs. The component of the strain tensor with the largest inhomogeneity is ε_{YZ}. The maps of ε_{YZ} in Fig. 6 are similar for primary grains G1, G2, G3 and their respective secondary grains G1′, G2′, G3′, revealing the accurate reliability of the strain analysis. The average of the component ε_{YZ} of the strain tensor is about $0.26\ 10^{-4}$, $-0.24\ 10^{-4}$, and $0.60\ 10^{-4}$ for primary grains G1, G2, and G3, respectively, and hence is nonuniform from one grain to the other. The maps of all of the components of the strain tensor are presented in Fig. 7(a) for grain G1. Importantly, all of the components of the strain tensor are strongly nonuniform and switch from compressive (i.e., negative) to tensile (i.e., positive) states within the same grain G1. The extrema of the strain tensor are located either
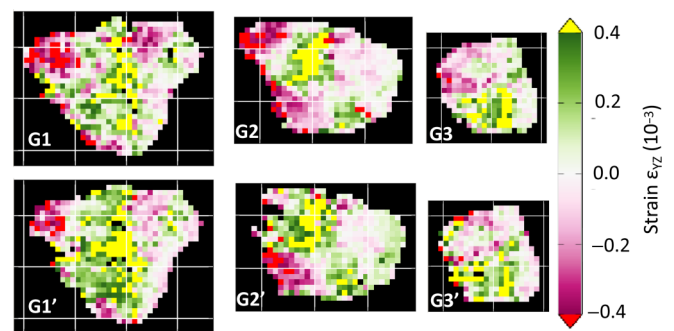

FIG. 6. (Color online) Maps of the strain component ε_{YZ} for primary grains G1, G2, and G3 and secondary grains G1′, G2′, and G3′. The high correlation in between primary and secondary grains indicates the accurate reliability of the strain and stress analysis.
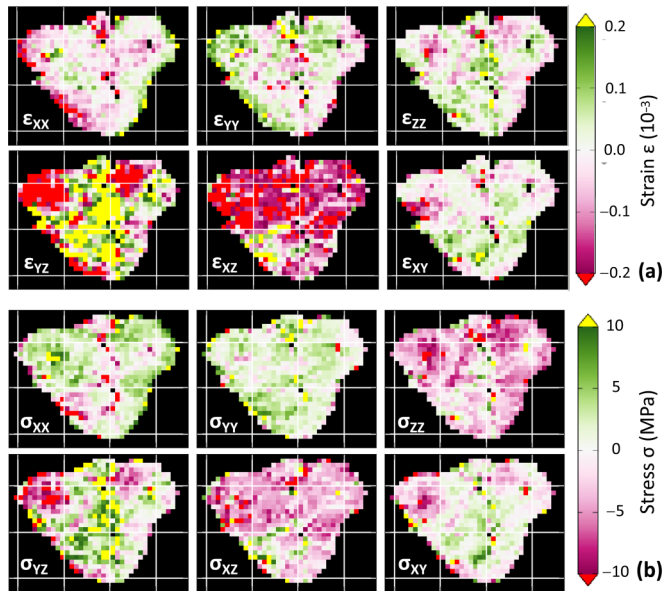
FIG. 7. (Color online) (a) Maps of the strain components ε_{XX}, ε_{YY}, ε_{ZZ}, ε_{YZ}, ε_{XZ}, and ε_{XY} for primary grain G1. (b) Maps of the stress components σ_{XX}, σ_{YY}, σ_{ZZ}, σ_{YZ}, σ_{XZ}, and σ_{XY} for primary grain G1. The z axis corresponds to the growth axis, while the x and y axes lie in the plane of the film. The y axis is horizontal in the map.

in the interior of grain G1 for the components ε_{YZ} and ε_{XZ} or in the vicinity of random GBs for the components ε_{XX} and ε_{YY}. The highly strained regions can thus be found either in the interior of the grains or in the vicinity of random GBs. The corresponding maps of all of the components of the stress tensor are revealed in Fig. 7(b). The largest inhomogeneity is also found for σ_{YZ}. The average of the component σ_{YZ} of the stress tensor is 1 ± 7 MPa, -1 ± 7 MPa, and 2 ± 5 MPa for primary grains G1, G2, and G3, respectively. The average is fairly small, while being associated with large standard deviations, since it is achieved with positive and negative stress values in the data analysis. The order of magnitude is, thus, smaller than the yield stress of several tens of megapascals in CdTe, which is consistent with the μ-Laue x-ray experiments operating within the elasticity theory. Despite the relatively low magnitude of the average of the component σ_{YZ}, a large variation of several tens of megapascals (i.e., 69 MPa for primary grain G1) arises within the same grain. Accordingly, the components ε_{YZ} and σ_{YZ} are highly nonuniform from one grain to the other but also within the grains themselves.

The physical origin for the unexpected strain nonuniformity can reasonably be understood in the light of the Volmer-Weber growth mechanism. In principle, it is not expected that random GBs can generate long-range strain and stress: according to standard theoretical models, the strain and stress fields associated with dislocation walls only spreads over several tens of nanometers [40,41]. Instead, grain-to-grain interactions may locally be involved during the growth of polycrystalline CdTe films following the Volmer-Weber-type mechanism, as discussed previously [3]. Importantly, the development of large columnar grains during the phase of secondary nucleation on top of preexisting stacked grains is expected to be strongly affected by the local environment of each of the grains through grain-to-grain interactions (i.e., collective effects) [27,42]:

the growth of each columnar grain is actually influenced by the growth of nearby columnar grains. These grain-to-grain interactions are likely to vary locally from one grain to the other even at a given film thickness, owing to the inhomogeneous spatial distribution of nucleation sites and to the spatial variation of growth conditions (i.e., growth temperature and flux). In particular, the variation of growth temperature and flux has a direct influence on the physical processes of adsorption, desorption, and diffusion of adatoms and hence of the formation of clusters with critical size. This results in the formation of grains with different shapes and sizes, as previously shown in Fig. 1; these can vary with film thickness but also in the plane of the film at a given film thickness. It is well-known that the size and shape of grains have a strong impact on the stress state and magnitude as well as on its spatial distribution. For instance, Nix *et al.* have shown that the magnitude of the biaxial stress generated during the phase of coalescence is inversely proportional to their radius [43]. In other words, any variation in the size and shape of grains that are coalescing and developing should result in the generation of biaxial stress with different magnitudes. Consequently, the mean magnitude of strain and stress is expected to vary from one grain to the other. Moreover, Gonzalez-Gonzalez *et al.* have recently shown theoretically in the framework of a multiscale approach that the spatial distribution of strain and stress can be nonuniform in the interior of growing grains [42]. Spolenak *et al.* have experimentally reported that grain-to-grain interactions occur in polycrystalline Al thin films and can account for the inhomogeneous spatial distribution of strain and stress in the interior of the grains: collective effects have been proposed as critical phenomena as grain growth proceeds [27]. Several other phenomena related to chemical effects are also expected to play a major role. For instance, chlorine atoms and cadmium vacancies segregate at random GBs in polycrystalline CdTe films [20]. The migration of impurities and intrinsic point defects at random GBs and on the surface could partially relieve the high biaxial stress previously induced by the phases of coalescence and postcoalescence [42,44,45]. Additional recrystallization phenomena may also be involved [42]. These may account for the spatial nonuniformity of the strain and stress components measured here and for their small average [31,42,44,45].

Also, CdTe, similar to most II-VI compound SCs, has a high ionicity of 0.7 on the Philips scale and thus is piezoelectric with a fairly large piezoelectric constant e_{14} of 0.04 C/m^2 [46,47]. Accordingly, the highly inhomogeneous local strain and stress might play a role on the local band bending by direct piezoelectric effects, which needs further developments in the theoretical model of the double Schottky potential barriers. Therefore, the characteristics of the local band bending at random GBs strongly depend on the nature of random GBs and also on the local environment in between nearby grains: the density of unpaired dislocations as well as the spatial distribution of strain and stress are critical on the local scale.

IV. CONCLUSION

The structural morphology of polycrystalline CdTe films strongly depends on film thickness. Stacked grains with

different sizes and shapes, including $\Sigma 3$ deformation twins, prevail for film thickness below 80–100 μm, and the evolution of their orientation can be explained by thermodynamic considerations. For film thickness above 80–100 μm, polycrystalline CdTe films exhibit larger columnar grains with a strong $\langle 111 \rangle$ texture and present a high density of $\Sigma 3$ growth twins and of random GBs, with the latter acting as nonradiative recombination centers. It is shown that the local band bending occurs at random GBs and its characteristics vary from one grain to the other. Such a variation is mostly due to the dependence of the local band bending on the nature of GBs and on the doping level in the nearby grains, in agreement with the theoretical model of the double Schottky potential barriers. Accordingly, no local band bending occurs at $\Sigma 3$ growth twins, as these extended defects do not have any dangling bonds in their center. Furthermore, it is revealed that the density of unpaired dislocations and the magnitude of the components of the strain and stress tensors are highly inhomogeneous from one grain to the other and in the interior of the grains themselves. This indicates that strong grain-to-grain interactions (i.e., collective effects) operate during the

Volmer-Weber-type growth. The nonuniformity could play a role on the spatial distribution of dopants as well as on the local band bending at GBs through direct piezoelectric effects. These findings stress the crucial importance of GB design engineering for enhancing the performances of solar cells and γ- and x-ray detectors made from polycrystalline CdTe films. To a broader extent, they highlight how polycrystalline compound SC films are ordered and behave locally as well as they emphasize the critical complexity of the local physical processes driving their performances on a larger macroscopic scale.

[1] S. M. Sze, *Semiconductor Devices Physics and Technology* (Wiley, New York, 1985).

[2] S. M. Sze, *Semiconductor Sensors* (Wiley, New York, 1994).

[3] C. V. Thompson, Annu. Rev. Mater. Sci. **30**, 159 (2000).

[4] C. R. M. Grovenor, J. Phys. C **18**, 4079 (1985).

[5] F. Greuter and G. Blatter, Semicond. Sci. Technol. **5**, 111 (1990).

[6] R. L. Petritz, Phys. Rev. **104**, 1508 (1956).

[7] J. Y. W. Seto, J. Appl. Phys. **46**, 5247 (1975).

[8] G. E. Pike and C. H. Seager, J. Appl. Phys. **50**, 3414 (1979).

[9] G. Blatter and F. Greuter, Phys. Rev. B **33**, 3952 (1986).

[10] I. Visoly-Fisher, S. R. Cohen, A. Ruzin, and D. Cahen, Adv. Mater. **16**, 879 (2004).

[11] I. Visoly-Fisher, S. R. Cohen, K. Gartsman, A. Ruzin, and D. Cahen, Adv. Funct. Mater. **16**, 649 (2006).

[12] J. Britt and C. Ferekides, Appl. Phys. Lett. **62**, 2851 (1993).

[13] M. A. Green, K. Emery, Y. Hishikawa, W. Warta, and E. D. Dunlop, Prog. Photovolt: Res. Appl. **22**, 1 (2014).

[14] P. J. Sellin, Nucl. Instrum. Methods A **563**, 1 (2006).

[15] T. P. Thorpe, A. L. Fahrenbruch, and R. H. Bube, J. Appl. Phys. **60**, 3622 (1986).

[16] J. Dutta, R. Pal, S. K. Bhattacharyya, S. Chaudhuri, and A. K. Pal, Mater. Chem. Phys. **36**, 177 (1993).

[17] J. Dutta, D. Bhattacharyya, A. B. Maiti, S. Chaudhuri, and A. K. Pal, Vacuum **46**, 17 (1995).

[18] M. J. Romero, M. M. Al-Jassim, R. G. Dhere, F. S. Hasoon, M. A. Contreras, T. A. Gessert, and H. R. Moutinho, Prog. Photovoltaics **10**, 445 (2002).

[19] V. Consonni, G. Feuillet, J. Bleuse, and F. Donatini, J. Appl. Phys. **101**, 063522 (2007).

[20] V. Consonni, G. Feuillet, J. P. Barnes, and F. Donatini, Phys. Rev. B **80**, 165207 (2009).

[21] V. Consonni and G. Feuillet, J. Cryst. Growth **316**, 1 (2011).

[22] I. Visloy-Fisher, S. R. Cohen, A. Ruzin, and D. Cahen, Appl. Phys. Lett. **82**, 556 (2003).

[23] P. Sutter, E. Sutter, and T. R. Ohno, Appl. Phys. Lett. **84**, 2100 (2004).

[24] S. Smith, P. Zhang, T. Gessert, and A. Mascarenhas, Appl. Phys. Lett. **85**, 3854 (2004).

[25] K. Durose, D. Boyle, A. Abken, C. J. Ottley, P. Nollet, S. Degrave, M. Burgelman, R. Wendt, J. Beier, and D. Bonnet, Phys. Status Solidi B **229**, 1055 (2002).

[26] N. Tamura, A. A. MacDowell, R. Spolenak, B. C. Valek, J. C. Bravman, W. L. Brown, R. S. Celestre, H. A. Padmore, B. W. Batterman, and J. R. Patel, J. Synchrotron Rad. **10**, 137 (2003).

[27] R. Spolenak, W. L. Brown, N. Tamura, A. A. MacDowell, R. S. Celestre, H. A. Padmore, B. Valek, J. C. Bravman, T. Marieb, H. Fujimoto, B. W. Batterman, and J. R. Patel, Phys. Rev. Lett. **90**, 096102 (2003).

[28] M. A. Phillips, R. Spolenak, N. Tamura, W. L. Brown, A. A. MacDowell, R. S. Celestre, H. A. Padmore, B. W. Batterman, E. Arzt, and J. R. Patel, Micro. Eng. **75**, 117 (2004).

[29] O. Ulrich, X. Biquard, P. Bleuet, O. Geaymond, P. Gergaud, J. S. Micha, O. Robach, and F. Rieutord, Rev. Sci. Instrum. **82**, 033908 (2011).

[30] J. S. Micha and O. Robach, Open-source LaueTools software, http://sourceforge.net/projects/lauetools/.

[31] V. Consonni, G. Feuillet, and P. Gergaud, J. Appl. Phys. **103**, 063529 (2008).

[32] C. Cayron, Acta Mater. **59**, 252 (2011).

[33] V. Consonni and G. Feuillet, J. Appl. Phys. **105**, 083535 (2009).

[34] Y. Yan, M. M. Al-Jassim, and T. Demuth, J. Appl. Phys. **90**, 3952 (2001).

[35] V. Consonni, G. Feuillet, and S. Renet, J. Appl. Phys. **99**, 053502 (2006).

[36] Y. Yan, M. M. Al-Jassim, and K. M. Jones, J. Appl. Phys. **94**, 2976 (2003).

[37] A. N. Pikhtin and A. D. Yas'kov, Sov. Phys. Semicond. **22**, 613 (1988).

[38] O. Vigil-Galan, L. Valliant, R. Mendoza-Perez, G. Contreras-Puente, and J. Vidal-Larramendi, J. Appl. Phys. **90**, 3427 (2001).

[39] N. Baïer, A. Brambilla, G. Feuillet, A. Lohstroh, S. Renet, and P. Sellin, Nucl. Instrum. Methods A **576**, 5 (2007).

[40] J. P. Hirth and J. Lothe, *Theory of Dislocations* (Wiley, New York, 1982).

[41] A. A. Nazarov, A. E. Romanov, and R. Z. Valiev, Acta Metall. **41**, 1033 (1993).

[42] A. Gonzalez-Gonzalez, C. Polop, and E. Vasco, Phys. Rev. Lett. **110**, 056101 (2013).

[43] W. D. Nix and B. M. Clemens, J. Mater. Res. **14**, 3467 (1999).

[44] E. Chason, B. W. Sheldon, L. B. Freund, J. A. Floro, and S. J. Hearne, Phys. Rev. Lett. **88**, 156103 (2002).

[45] J. S. Tello, A. F. Bower, E. Chason, and B. W. Sheldon, Phys. Rev. Lett. **98**, 216104 (2007).

[46] N. E. Christensen, S. Satpathy, and Z. Pawlowska, Phys. Rev. B **36**, 1032 (1987).

[47] A. Dal Corso, R. Resta, and S. Baroni, Phys. Rev. B **47**, 16252 (1993).